RADIAL STAR FORMATION HISTORIES IN FIFTEEN NEARBY GALAXIES

Daniel A. Dale[1], Gillian Beltz-Mohrmann[2], Arika Egan[3] Alan Hatlestad[1], Laura Herzog[4], Andrew Leung[5], Jacob McClane[6] Christopher Phenicie[7], Jareth Roberts[1], Kate Barnes[8], Médéric Boquien[9], Daniela Calzetti[10], Henry A. Kobulnicky[1], Shawn Staudaher[1], and Liese van Zee[8]

ABSTRACT

New deep optical imaging is combined with archival ultraviolet and infrared data for fifteen nearby galaxies mapped in the *Spitzer* Extended Disk Galaxy Exploration Science survey. These images are particularly deep and thus excellent for studying the low surface brightness outskirts of these disk dominated galaxies with stellar masses ranging between 10^8 and 10^{11} $M_\odot$. The spectral energy distributions derived from this dataset are modeled to investigate the radial variations in the galaxy colors and star formation histories. Though there is substantial variation from galaxy to galaxy, taken as a whole the sample shows bluer and younger stars for larger radii until reversing near the optical radius, whereafter the trend is for redder and older stars for larger galacto-centric distances. These results are consistent with an inside-out disk formation scenario coupled with an old stellar halo formed through radial migration of bulge stars to the outer disk and/or the cumulative history of minor mergers and accretions of satellite dwarf galaxies.

Subject headings: ISM: general — galaxies: ISM — infrared: ISM

---

[1]Department of Physics & Astronomy, University of Wyoming, Laramie, WY 82071; ddale@uwyo.edu

[2]Department of Physics, Wellesley College, Wellesley, MA 02481

[3]Department of Physics, Northern Michigan University, Marquette, MI 49855

[4]Department of Physics & Astronomy, Minnesota State University, Moorhead MN 56563

[5]Department of Physics & Astronomy, Rutgers University, Piscataway, NJ, 08854

[6]Department of Physics & Astronomy, Northern Arizona University, Flagstaff, AZ 86011

[7]School of Physics & Astronomy, University of Minnesota, Minneapolis, MN 55455

[8]Department of Astronomy, Indiana University, Bloomington, IN 47405

[9]Institute of Astronomy, University of Cambridge, Madingley Road, Cambridge CB3 0HA, UK

[10]Department of Astronomy, University of Massachusetts, Amherst, MA 01003, USA

1. Introduction

Understanding how galaxies assemble is crucial to understanding the overall picture of galaxy evolution. In ΛCDM models, galactic disks are built through mergers and the accretion of small satellites, as well as through *in situ* star formation activity (e.g., Abadi et al. 2003; Governato et al. 2004; Robertson et al. 2006; Governato et al. 2007). In the "inside-out" scenario, galaxy disks systematically grow through star formation in the outermost parts. This process should manifest itself with specific observable hallmarks easily obtained from ground-based campaigns, including gradients in metallicity and specific star formation rates coupled with longer disk scale lengths for younger stellar populations and thus increasingly blue colors at larger radii (Larson 1976; Ryder & Dopita 1994; Avila-Reese & Firmani 2000; de Jong 1996; MacArthur et al. 2004; Muñoz-Mateos et al. 2007; Wang et al. 2011; Barnes et al. 2014). Resolved stellar photometry can also help provide clues to the formation history of spiral galaxies (e.g., Brown et al. 2008; Monachesi et al. 2013). Analysis of star formation histories via *Hubble Space Telescope*-based color-magnitude diagrams for NGC 300 and M 33 indicate an inside-out formation scenario, with decreasing metallicity and stellar age for larger radii within the galaxy disks, and then a reversal to positive stellar age gradients for the outer portions of M 33 (Williams et al. 2009; Gogarten et al. 2010; Barker et al. 2011). Galaxy-wide outside-in disk formation, on the other hand, has only been plausibly suggested for dwarf galaxies, galaxies for which their low masses leave them more susceptible to environmental effects (e.g., Zhang et al. 2012).

Investigations that concentrate on the outermost parts of galaxies can yield additional information on the galaxy formation process (e.g., Ferguson et al. 1998; Thilker et al. 2007). For example, Pohlen & Trujillo (2006) find that later-type spiral galaxies are more likely to exhibit downbending, where the outer surface brightness profile more steeply drops than the surface brightness profile of the main disk, and earlier-type spirals are more likely to have outer upbending profiles. Simulations predict this upbending phenomenon in galaxies with significant accretion histories (Abadi et al. 2006). The Keck-based work of Ibata et al. (2005) finds stars kinematically associated with M 31 as far as 70 kpc ($1.6a_{25}$[1]) from the galaxy center, located in complex, ephemeral substructures suggestive of prior accretion. Similarly, Herbert-Fort et al. (2009) use deep LBT optical and GALEX ultraviolet imaging to probe the blue and red stellar populations in NGC 3184 out to and beyond $1.6a_{25}$. In this galaxy red stellar clusters are more prominent than their blue counterparts at the largest radii; the authors posit that the the stellar clusters at the outer edge of the main stellar disk are

[1] a_{25} is defined as the length of the semi-major axis for the B-band isophote at 25 mag arcsec^{-2} (de Vaucouleurs et al. 1991).

a natural extension of the spiral arms whereas the outermost stellar clusters likely arrived via past accretion events (see also Herbert-Fort et al. 2012). The presence of older stars in a galaxy's periphery could arise through internal dynamical processes that redistribute stars originally formed near the center (e.g., "radial migration" Sellwood & Binney 2002; Roškar et al. 2008; Radburn-Smith et al. 2012). Alternatively, simulations suggest that the stellar haloes of galaxies arise from the cumulative history of hierarchical merging and very little stemming from in situ star formation (Abadi et al. 2006; Read et al. 2006; Purcell et al. 2007; Cooper et al. 2013). If these accretion events are largely ancient (e.g., Bullock & Johnston 2005; Abadi et al. 2006) then passive stellar evolution will naturally result in predominantly red stellar haloes. To help disentangle which of the various processes are the main drivers in building up galaxy disks and haloes, it is necessary to construct a robust, wide-field, and multi-wavelength dataset for constraining galaxy surface brightness profiles, extinctions, metallicities, and overall star formation histories.

Here we report on a multi-wavelength analysis of 15 nearby galaxies drawn from the Extended Disk Galaxy Exploration Science (EDGES) survey (van Zee et al. 2012). One of the primary goals of EDGES is to probe the extent of the old stellar population as far out as possible with *Spitzer*, and to compare those extents at other wavelengths tracing other emission mechanisms. In this effort we combine the 3.6 μm EDGES data with new deep, ground-based optical and archival space-based ultraviolet and infrared imaging to constrain the radial trends in the star formation histories of these 15 galaxies. The depth of our imaging dataset enables a careful investigation in particular of the galaxy outskirts, where the low surface brightness levels typically are a challenge to detect with sufficient signal-to-noise. The mid- and far-infrared data utilized in this analysis allow the SED fits to be carried out in an energy-balanced fashion: any ultraviolet/optical light that is modeled to be extinguished by dust reappears at longer wavelengths as dust emission. Previous EDGES work includes Barnes et al. (2014), who utilize 3.6 μm, H I, and far-ultraviolet data to characterize the full disk and associated streamer for NGC 5236 (M 83), Richards (2015) combine H I and 3.6 μm data with optical imaging and spectroscopy to constrain a dark matter halo model for NGC 5005, and Staudaher. (2015a) use the 3.6 μm data to quantify the stellar halo mass fraction of NGC 5055 (M 63) and the mass of its prominent tidal feature. A detailed study of the 3.6 μm surface brightness profiles will be presented in Staudaher. (2015b).

Section 2 presents the sample studied here, Section 3 reviews the new and archival data compiled for this analysis along with an overview of the data processing, Section 4 explains the analysis including the fitting of the spectral energy distributions (SEDs), Section 5 presents the main results, and Section 6 provides a summary and brief discussion.

2. Galaxy Sample

Table 1 provides the list of galaxies studied here. They represent a subset of EDGES galaxies observable during the summer of 2014 from the Wyoming Infrared Observatory (WIRO) and served as the centerpiece of the work carried out by the 2014 cohort of Wyoming REU (Research Experience for Undergraduates) interns. Priority was given to targets with good ancillary ultraviolet and infrared data (§ 3). The overall EDGES sample contains 92 nearby galaxies spanning a range of morphology, luminosity, and environment, for galaxies at high Galactic latitudes $|b| > 60°$, with apparent magnitudes $m_B < 16$, and optical angular diameters $2 \lesssim D(') \lesssim 13$. Included in the list of 15 galaxies studied here is one non-EDGES "Target of Opportunity" galaxy, NGC 4625, which happened to fall within the field-of-view of our NGC 4618 observations. Two of the galaxies in this subset of EDGES have S0 morphology, four are irregulars, and the remainder are spiral galaxies. All 15 galaxies lie within ~ 20 Mpc.

3. Data

3.1. *Spitzer* 3.6 μm Data

For the EDGES sample we constructed large mosaics based on *Spitzer Space Telescope* imaging that trace 3.6 and 4.5 μm substructures out to at least five times the optical radius a_{25}. Compared to most *Spitzer*/IRAC imaging campaigns of nearby galaxies, the EDGES near-infrared image mosaics are quite deep; the 1800 s integration per position obtained for EDGES targets is 7.5 times longer than what was obtained for the SINGS (Kennicutt et al. 2003), LVL (Dale et al. 2009), and S^{4}G (Sheth et al. 2010) surveys, and 12–30 times longer compared to the IRAC GTO project (Pahre et al. 2004). We reach a 1σ per pixel sensitivity of 2 kJy sr^{-1}, and averaging over several square arcminutes can reach down to below 0.4 kJy sr^{-1} (fainter than 29 mag arcsec^{-2} AB), a level necessary for securely detecting faint stellar streams associated with nearby galaxies (Krick et al. 2011; Barnes et al. 2014; Staudaher. 2015a). For comparison, *WISE* achieves a 3.4 μm diffuse sensitivity larger than 1 kJy sr^{-1} over a $5' \times 5'$ area (Wright et al. 2010).

3.2. Ancillary Ultraviolet and Infrared Data

Archival ultraviolet and infrared data were gathered from the *GALEX*, *Spitzer*, *WISE*, and *Herschel Space Observatory* archives. In all instances, priority was given to longer-

exposure data, where available. As such, the ultraviolet data for only two galaxies (see Table 2) stem exclusively from the shallow All-Sky Imaging Survey for which the integrations are ∼0.1 ks (Martin et al. 2005); the majority of the GALEX imaging utilized here arises from integrations longer than 1 ks. Likewise, most of the infrared data derives from sensitive *Spitzer* 24 μm imaging of warm dust emission from the Local Volume Legacy (Dale et al. 2009), with *WISE* 22 μm and *Herschel* 70 μm used to fill in any gaps. These ancillary/archival datasets have angular resolutions of $\sim 5-6''$.

3.3. New Optical Observations and Data Processing

New deep $u'g'r'$ imaging was obtained on the WIRO 2.3 m telescope with the WIRO-Prime camera (Pierce & Nations 2002) over the course of the summer of 2014. For each galaxy and each filter 12 individual 300 s frames were taken. Individual frames were randomly dithered with small offsets for enhanced pixel sampling. Each night a series of zero second bias frames were obtained in addition to a series of twilight sky flats within each filter.

The optical images were processed with standard procedures, including subtraction of a master bias image and removal of pixel-to-pixel sensitivity variations through flatfield corrections. Typically the sky flat was constructed from flats taken on the same night, but occasionally flats from multiple consecutive nights were utilized. The 12 dithered 300 s frames for a galaxy taken in one filter were aligned and stacked, resulting in images with integrations equivalent to one hour. The stacked images are flat to 1% or better on $10'$ scales. The astrometric solutions and flux zeropoints were calibrated using positions and photometry extracted from Sloan Digital Sky Survey (SDSS; York et al. 2000) imaging on several foreground stars spread across each image stack. The uncertainties in the zeropoint calibrations were typically 2%. The 5σ $u'g'r'$ point source sensitivities are ∼23.0, 24.0, 23.4 mag for $2\farcs8$ diameter apertures (twice the seeing FWHM), about 1–1.8 magnitudes deeper than SDSS (e.g., sdss.org/dr12/scope; Cook et al. 2014). Conspicuous foreground stars and background galaxies were removed from each image using IRAF/`IMEDIT` and a local sky interpolation. Of particular note is the bright foreground star superposed on the nucleus of NGC 4707. This star was edited in the u', g', r', and 3.6 μm images. Additionally, the overlap region between NGC 4485 and NGC 4490 was edited. Fortunately this region is fractionally small compared to the total areas within the outermost elliptical annuli: approximately $\frac{1}{4}$ for NGC 4485 and $\frac{1}{8}$ for NGC 4490.

4. Data Analysis

To facilitate a consistent panchromatic analysis, the higher angular resolution data ($u'g'r'$, 3.6 μm) were smoothed (using a Gaussian smoothing profile) to the $\sim$6$''$ resolution of the ultraviolet and mid-infrared data. However, an identical analysis using the images at their native resolutions yields similar end results described in § 5, due in large part to the relatively coarse annular apertures utilized (see § 4.1). A local sky value was estimated and removed via several apertures located just beyond the outermost reaches of the galaxy emission; care was taken to include a typical distribution of foreground stars within the sky apertures, in order to better account for the presence of foreground stars within the galaxy apertures (Figure 1). Note that if a representative sampling of foreground stars is *not* included in the sky apertures, the inferred flux for each on-source aperture will be underestimated and with a fractionally significant impact for the faintest regions in the galaxy outskirts.

4.1. Elliptical Photometry

Photometry was obtained for each galaxy using IRAF/`IMCNTS` and a series of elliptical annuli covering semi-major axis a ranges of $0<\frac{a}{a_{25}}<0.25$, $0.25<\frac{a}{a_{25}}<0.5$, $0.5<\frac{a}{a_{25}}<0.75$, $0.75<\frac{a}{a_{25}}<1$, $1<\frac{a}{a_{25}}<1.25$, and $1.25<\frac{a}{a_{25}}<1.5$. For the range of galaxy angular sizes in our sample, these $\frac{1}{4}a_{25}$ annular widths correspond to a range of values between 14$''$ (for UGC 7301) and 94$''$ (for NGC 5055). Traditional surface brightness analyses typically rely on a finer set of annular widths, but any analysis that requires a full panchromatic dataset (e.g., SED fitting) is necessarily limited by the wavelength for which the detected extent of the emission is smallest. Our choice of coarsely-spaced annular apertures provides less spatial information but allows for more robust signal-to-noise in the galaxy outskirts where the emission is weakest. All annuli for a given galaxy used the same (NED-based) centroids, position angles, and ellipticities. Photometric uncertainties $\epsilon_{\rm total}$ are computed by summing in quadrature the calibration error $\epsilon_{\rm cal}$ and the measurement uncertainty $\epsilon_{\rm sky}$ based on the measured sky fluctuations, i.e.,

$$\epsilon_{\rm total} = \sqrt{\epsilon_{\rm cal}^2 + \epsilon_{\rm sky}^2} \quad (1)$$

with

$$\epsilon_{\rm sky} \ = \sigma_{\rm sky}\Omega_{\rm pix}\ \sqrt{N_{\rm pix} + {N_{\rm pix}}^2/N_{\rm sky}} \quad (2)$$

where $\sigma_{\rm sky}$ is the standard deviation of the sky surface brightness fluctuations, $\Omega_{\rm pix}$ is the solid angle subtended per pixel, and $N_{\rm pix}$ and $N_{\rm sky}$ are the number of pixels in an annulus and (the sum of) the sky apertures, respectively. All fluxes were corrected for Galactic extinction (Schlafly & Finkbeiner 2011) assuming $A_V/E(B-V) \approx 3.1$ and the reddening curve of Draine (2003).

4.2. SED Fitting

The full ultraviolet–infrared SEDs were fitted using the Bayesian-based CIGALE software package (Noll et al. 2009; Boquien 2015; Burgarella 2015). This package allows the user to estimate fundamental parameters such as stellar mass, star formation rate, and the characteristic epoch of star formation and its decay rate using an energy-balanced approach whereby the diminution of ultraviolet/optical light via dust extinction is accounted for in equal amounts in the infrared via dust emission. In our SED fitting we adopt the stellar and dust emission libraries of Bruzual & Charlot (2003) and Dale et al. (2014), respectively, the Chabrier (2003) stellar initial mass function, and a dust attenuation curve based on the work of Calzetti et al. (2000) and Leitherer et al. (2002). The fit parameters include metallicity, extinction, attenuation curve modifier, and characteristics of the major star-forming events. For example, a double exponential star formation history would be modeled as

$$SFR(t) \propto \mathcal{A}_1 e^{-(t-t_1)/\tau_1} + \mathcal{A}_2 e^{-(t-t_2)/\tau_2}, \quad \mathcal{A}_1(t-t_1<0)=0, \mathcal{A}_2(t-t_2<0)=0 \quad (3)$$

where the first term represents a standard exponentially decaying star formation event beginning at time t_1 with e-folding time τ_1 and amplitude $\mathcal{A}_1$, and the second term represents a later burst of star formation beginning at time t_2 with e-folding time τ_2 and amplitude $\mathcal{A}_2$ (Papovich et al. 2001; Borch et al. 2006; Gawiser et al. 2007; Lee et al. 2009). Another form of star formation history we utilize here is the so-called delayed star formation history model (Lee et al. 2010, 2011; Schaerer et al. 2013), i.e.,

$$SFR(t) \propto \mathcal{A}_0 t e^{-(t-t_0)/\tau}, \quad \mathcal{A}_0(t-t_0<0)=0. \quad (4)$$

Unlike the double exponential star formation history for which the maxima occur at $t-t_1=0$ and $t-t_2=0$, in this formulation the maximum star formation rate occurs at the value of the e-folding rate after the onset of star formation: $t-t_0=\tau_0$. Figure 2 shows the characteristics of four example delayed star formation models in addition to an example of a double exponential model. Note how smaller values of τ_0 correspond to more sharply defined and earlier characteristic epochs of star formation. Both of the above prescriptions for star formation histories are utilized in this work, but the use of a delayed star formation model is preferred since it is a simple prescription that relies on a small number of parameters and CIGALE-based simulations show that it can accurately recover (to within 10%) galaxy stellar masses and star formation rates (Buat et al. 2014; Ciesla et al. 2015).

The input parameter ranges are provided in Table 3. The main output physical parameters (e.g., M_*, τ, A_V) are computed based on a probability distribution function (PDF) analysis: the SED fit χ^2 is derived for each combination of input parameters, a PDF is constructed for each parameter based on the χ^2 for the best fit models, and the probability-

weighted means and standard deviations of the PDFs are adopted as the values and associated uncertainties of the output physical parameters (see § 2.2 of Noll et al. (2009) for details of the process).

5. Results

5.1. Directly Observed: Fluxes

Table 4 provides the integrated fluxes arising from within the $2a_{25} \times 2b_{25}$ apertures. For the subset of the sample that has published data, spanning nine galaxies and seven wavelengths, these fluxes agree quite well with published values: the average ratio of these fluxes to literature fluxes is 0.98 ± 0.02. Two notable exceptions are for the GALEX measurements of NGC 4625, a galaxy with known extended ultraviolet emission (Thilker et al. 2007).

5.2. Directly Observed: Surface Brightness Profiles and Optical Colors

Figure 3 displays the surface brightness profiles for the seven different wavelengths observed for each galaxy. The profiles generally fall with radius, though for a few galaxies the peak of the warm dust emission (usually traced by MIPS 24 μm) is significantly spatially displaced from the galaxy centers; the warm dust emission does not spatially mimic the stellar emission for NGC 4242, NGC 4485, UGC 8303, and NGC 5523. The dust emission surface brightness profile is also one of two profiles that is not systematically detected sample-wide out to the last annular region of $1.25<a/a_{25}<1.50$; the (detection of the) dust emission is truncated for NGC 4420, NGC 4242, NGC 4625, UGC 8320, NGC 5273, and NGC 5608 (the far-ultraviolet is also undetected for the last annular region of NGC 4220). Many galaxies show fairly consistent profile shapes in the ultraviolet/optical/near-infrared, but we note that the two most inclined galaxies in our sample, UGC 7301 ($b/a = 0.13$) and NGC 5229 ($b/a = 0.17$), exhibit the smallest scatters in the surface brightness profile (log-linear) slopes $m(\lambda) = \Delta \log I_\nu(\lambda)/\Delta(a/a_{25})$, with $\sigma(m) = 0.05$ dex and 0.08 dex for UGC 7301 and NGC 5229, respectively. This similarity in slopes across wavelengths for the more inclined systems is not the result of reddening effects, since the internal extinctions derived in the SED fitting (§ 4.2) are not unusually large for UGC 7301 and NGC 5229. Rather, the similarity is more likely due to the projected mixing of inner and outer disk regions for the central annular apertures. The less inclined galaxies show nuanced differences in their multi-wavelength surface brightness profiles, which in turn lead to variations in the color profiles and in the interpreted star formation histories, as discussed below.

Pohlen & Trujillo (2006) studied the g' and r' surface brightness profiles of 85 moderately inclined, late-type spiral galaxies from SDSS. Martín-Navarro et al. (2012) carried out a similar study for 34 inclined galaxies using SDSS and *Spitzer* 3.6 μm images. Pohlen & Trujillo (2006) found that 60% (30%) of their systems displayed exponential disks followed by downbending (upbending) surface brightness profiles; Martín-Navarro et al. (2012) found generally similar results. They saw downbending features primarily for later-type spiral galaxies and upbending for earlier-type spirals. Our relatively coarse annular sampling may not yield surface brightness profiles as detailed as those studied by Pohlen & Trujillo (2006), but we can explore any trends near the galaxy outskirts with higher signal-to-noise, especially since our images go significantly deeper (§ 3.3). Our multi-wavelength collection of surface brightness profiles in Figure 3 exhibit all three types of profiles. However, only two of our targets satisfy the Pohlen & Trujillo (2006) joint criteria of late-type spiral morphology ($3 \leq T \leq 8$) and moderately inclined ($b/a > 0.5$), so no strong conclusions based on going significantly deeper than SDSS can be drawn here.

On the other hand, stacking the images of many galaxies can yield exquisitely sensitive surface brightness profiles (e.g., Zibetti et al. 2004; Tal & van Dokkum 2011). Though such analyses cannot provide insight on individual systems, they do inform us about the broad brush characteristics for large ensembles of galaxies. D'Souza et al. (2014) stack the g' and r' SDSS images for over 45,000 isolated galaxies at redshifts $0.05 \leq z \leq 0.1$. Binned according to global galaxy stellar mass, their stacks probe down to an effective surface brightness of $\mu(r) \sim 32$ mag arcsec^{-2} (compared to 27 mag arcsec^{-2} for Pohlen & Trujillo 2006). They find that the stacked stellar profiles steepen for more massive galaxies, and they separate their analysis into high and low concentration systems (see their Figure 8). We find a similar steepening of the slopes of the 3.6 μm surface brightness profiles over the stellar mass range probed here ($< 10^{11}$ $M_{\odot}$). The result holds for all ultraviolet, optical, and near-infrared wavelengths, but we focus on the 3.6 μm slopes in Figure 4 to avoid complications at shorter wavelengths due to attenuation by dust.

D'Souza et al. (2014) also find that the outer portions, which they refer to as the stellar halos, are redder than the main disk for all systems with $M_* < 10^{11}$ $L_{\odot}$, and that the detected halo mass fraction rises with increasing galaxy mass. This reddening feature is not due to effects of dust attenuation since galaxy dust mass surface densities are minimal for larger radii (Muñoz-Mateos et al. 2009; Aniano et al. 2012). Figure 5 presents a compilation of the radial $g' - r'$ trends for our sample. Our galaxies exhibit a similar range in $g' - r'$ color as seen in the SDSS stacks, but there is considerable scatter between galaxies (see also West et al. 2009; Tortora et al. 2010). Considered as a whole, though, our sample shows an outward reddening color trend (upper panel of Figure 6); on average, our galaxies are redder at $a = 1.13a_{25}$ by 0.1 mag in $g' - r'$ compared to the value at $a = 0.63a_{25}$. D'Souza et al.

(2014) suggest such peripheral reddening implies accretion of old stars into the stellar halo.

It has been shown that the extended wings of the Point Spread Function (PSF) can lead to artificially red colors for observations utilizing thinned CCDs (Michard 2002). This so-called "red halo" effect stems from increased instrumental scattering at longer wavelengths for radial distances greater than $\sim$15″, leading some authors to ignore SDSS i band data when studying galaxy colors: the effect is much less pronounced for the shorter-wavelength SDSS filters while the SDSS z band data are taken with unthinned CCDs and thus do not suffer from this effect (Wu et al. 2005; Liu et al. 2009). Though the WIROPrime camera utilizes a thinned detector, i band data were not utilized in this analysis. However, there is a second potential PSF-related issue: for inclined galaxies each line-of-sight contains emission from a range of galacto-centric distances, and the impact is of course largest for edge-on galaxies. We investigate these issues for UGC 7301, the smallest and most inclined galaxy in the sample. Figure 7 provides a comparison of $g' - r'$ colors for our annuli and for a series of 9″-diameter apertures placed along the major axis, an arrangement that promotes a more PSF-independent radial analysis. No obvious differences appear between the two color trends, and so annular smearing is expected to be negligible in this work. To enable further interpretation of the observed colors, we turn to SED fitting of the complete collection of panchromatic surface brightness profiles.

5.3. Inferred from SED Fitting: Star Formation Histories

An example of our SED fitting results is displayed in Figure 8 for NGC 4618, a galaxy for which dust emission is detected throughout the six annular regions studied. As described in § 4.2, multiple parameters are involved in such fits. Figure 9 presents for each galaxy the e-folding timescale radial trends for a delayed star formation history. We experimented with allowing t_0, the age of the oldest stars, to be a free parameter with a range of 6–13 Gyr ago. But the radial trends for τ_0 were essentially unchanged for different values of t_0, so we adopted a fixed value of $t_0 = 11$ Gyr ago in order to minimize the number of free parameters in the fits. As a result of fixing t_0, any differences in τ_0 directly correspond to differences in the timing of the peak of the star formation histories (see Figure 2 and the corresponding discussion in § 4.2). The error bars seen in Figure 9 are generally larger for larger values of τ_0, which can be visually deciphered from inspection of Figure 2: the profile of the delayed star formation model is broader for larger τ_0 and thus naturally leads to a less well constrained epoch for the peak in the star formation history. Similar to what is seen for the $g' - r'$ profiles, for some galaxies the τ_0 trend is essentially flat, for others it is mildly falling, there are galaxies that show rising-then-falling radial trends, etc. The two S0 galaxies, NGC 4220 and NGC 5273,

are notable in this presentation since they show the smallest and most constant values for τ_0. The implication is that the bulk of their stars formed spatially more uniformly across the disk, and with an earlier and more sharply defined epoch of star formation, than the stellar populations in the 13 other galaxies in the sample. When all the τ_0 values are presented in a single plot (lower panel of Figure 6), the sample overall shows older stellar populations stemming from more sharply defined epochs of star formation at both the galaxy centers and galaxy outskirts compared to the stellar populations at mid-galacto-centric distances. On average, our galaxies' characteristic epoch of star formation is ~ 2 Gyr earlier at $r = 0.13a_{25}$ and $1.38a_{25}$ compared to the value at $r = 0.63a_{25}$. Similar results are seen for the e-folding time τ_1 of the main stellar population when a double exponential star formation history is considered (Equation 3 and filled triangles in 6).

Older on both the inside and the outside is consistent with being redder in those locations (provided our constraints on dust reddening and metallicity are reasonable). Moreover, this scenario is consistent with what is seen observationally for M 33 and other nearby galaxies: an inside-out formation process for the main galaxy disk where the stars are younger and the colors increasingly blue with radius (e.g., González Delgado et al. 2014), followed by a redder and older stellar population in the galaxy peripheries or haloes (Williams et al. 2009; Gogarten et al. 2010; Barker et al. 2011). Bullock & Johnston (2005) find in their simulations of galaxy stellar halo formation that the bulk of the mass in haloes derives from the remnants of accreted satellites merger tidal debris that occurred on average 9 Gyr ago. During the time that has passed since those accretion events, the stars have passively evolved to provide an old, red present-day appearance for the spiral galaxy haloes. Alternatively, Roškar et al. (2008) and Sánchez-Blázquez et al. (2009) predict that radial migration, a process whereby the influence of passing spiral arms can transport stars outwards, results in a conspicuous old–young–old mean radial age profile, in essence creating a red stellar halo through internal dynamical processes. Though there is ample evidence that the outer disks of many galaxies possess pockets of active star formation (Gil de Paz et al. 2005; Thilker et al. 2007; Dong et al. 2008; Alberts et al. 2011), there are not enough OB stars in galaxy peripheries to result in overall blue stellar haloes.

While we are mainly interested in the e-folding timescales inferred from the SED fitting, it is important to verify that the other output physical parameters derived are reasonable, as a check on the overall fit reliability. The fitted metallicities range from half-solar to slightly super-solar, with higher values preferentially found near the galaxy optical centers. The extinction range is 0.1–1.1 mag in $A_V \approx 3.1E(B-V)^y_*$ and again the average value peaks, as expected, for the innermost annular regions. Figure 10 shows a comparison between the global star formation rates output from the CIGALE fits and those independently derived from a combination of the global Hα and 24 μm data, taking care to ensure that

both estimates use the same galaxy distances and initial mass function prescriptions (e.g., Equations 1 and 16 of Kennicutt et al. 2008). The average ratio of the two types of star formation rates is 0.94, with a dispersion of 0.4 and peak-to-peak variations within a factor of $\sim$2 from unity. To help further assess the validity of the SED fit parameters, a series of Monte Carlo simulations were carried out. In each simulation a random (Gaussian deviate) flux offset, scaled according to the measured uncertainty, was added to each flux. For each of these simulations the same SED fitting and Bayesian-based analysis described above was carried out. Figure 11 presents a comparison between the standard fit parameters and those from the Monte Carlo analysis. The standard deviation of the difference between the canonical and simulated e-folding time is about 700 Myr, a reasonable value given the estimated uncertainties. The output parameters with the broadest distributions in Figure 11 are the dust model power-law parameter α (see Dale et al. 2014) and the stellar metallicity Z: the simulated values for these parameters disperse noticeably more from the standard values, with standard deviations in each distribution of $\sim$0.2.

6. Summary and Discussion

The *Spitzer* EDGES survey provided large and extremely sensitive near-infrared maps for 92 nearby galaxies. We report here results for a subset of the EDGES sample based on EDGES and ancillary data in addition to a follow-up ground-based campaign for deep $u'g'r'$ imaging on the 2.3 m WIRO telescope. This panchromatic database is utilized to study radial trends in galaxy surface brightnesses, colors, and star formation histories, with a primary goal of taking advantage of the imaging depth in the outermost portions of the galaxies. The star formation histories are estimated using ultraviolet-optical-infrared SED fits executed in an energy-balanced fashion, whereby the ultraviolet/optical radiation attenuated by dust is converted in equal portions to dust emission in the infrared. While most surface brightness profiles peak at the galaxy centers and then systematically fall with radius, the dust profiles for four late-type systems peak off-center. In these systems the $g' - r'$ radial color trends are generally bluer, and the star formation history profiles younger, where the warm dust emission peaks suggesting that the dust is tracing sites of recent star formation. Similar to results from SDSS-based analyses of optical galaxy colors (D'Souza et al. 2014), we find that both the central and the outermost galaxy regions for the sample ensemble show redder colors than the mid-galactic radial regions. The star formation histories provide additional evidence, suggesting that these mid-galactic regions are on average younger than the central bulge and the galaxy peripheries. These results are consistent with disks forming in an inside-out fashion combined with an old and red stellar halo formed through contributions from either radial migration or the cumulative effect of past mergers and accretion events.

However, even though these data and this analysis present a coherent picture of star formation within nearby galaxies, there are significant variations on a galaxy-by-galaxy basis and thus a larger study encompassing a much larger fraction of the EDGES sample is warranted.

This work is supported by the National Science Foundation under REU grant AST 1063146. This work is based on observations made with the *Spitzer Space Telescope*, which is operated by the Jet Propulsion Laboratory, California Institute of Technology Support under a contract with NASA. Support for this work was provided by NASA through an award issued by the JPL/Caltech. *Herschel* is an ESA space observatory with science instruments provided by European-led Principal Investigator consortia and with important participation from NASA. This research has made use of the NASA/IPAC Infrared Science Archive, which is operated by the Jet Propulsion Laboratory, California Institute of Technology, under contract with NASA. We gratefully acknowledge NASA's support for construction, operation, and science analysis for the GALEX mission, developed in cooperation with the Centre National d'Etudes Spatiales of France and the Korean Ministry of Science and Technology. Funding for the Sloan Digital Sky Survey and SDSS-II has been provided by the Alfred P. Sloan Foundation, the Participating Institutions, the NSF, the U.S. Department of Energy, NASA, the Japanese Monbukagakusho, the Max Planck Society, and the Higher Education Funding Council for England.

REFERENCES

Abadi, M. G., Navarro, J. F., & Steinmetz, M. 2006, MNRAS, 365, 747

Abadi, M. G., Navarro, J. F., Steinmetz, M., & Eke, V. R. 2003, ApJ, 597, 21

Alberts, S., Calzetti, D., Dong, H., et al. 2011, ApJ, 731, 28

Aniano, G., Draine, B. T., Calzetti, D., et al. 2012, ApJ, 756, 138

Avila-Reese, V., & Firmani, C. 2000, Rev. Mexicana Astron. Astrofis., 36, 23

Barker, M. K., Ferguson, A. M. N., Cole, A. A., et al. 2011, MNRAS, 410, 504

Barnes, K. L., van Zee, L., Dale, D. A., et al. 2014, ApJ, 789, 126

Boquien, M. 2015, MNRAS, in prep

Borch, A., Meisenheimer, K., Bell, E. F., et al. 2006, A&A, 453, 869

Brown, T. M., Beaton, R., Chiba, M., et al. 2008, ApJ, 685, L121

Bruzual, G., & Charlot, S. 2003, MNRAS, 344, 1000

Buat, V., Heinis, S., Boquien, M., et al. 2014, A&A, 561, A39

Bullock, J. S., & Johnston, K. V. 2005, ApJ, 635, 931

Burgarella, D. 2015, A&A, in prep

Calzetti, D., Armus, L., Bohlin, R. C., et al. 2000, ApJ, 533, 682

Chabrier, G. 2003, PASP, 115, 763

Ciesla, L., Charmandaris, V., Georgakakis, A., et al. 2015, ArXiv e-prints, arXiv:1501.03672

Cook, D. O., Dale, D. A., Johnson, B. D., et al. 2014, MNRAS, 445, 881

Cooper, A. P., D'Souza, R., Kauffmann, G., et al. 2013, MNRAS, 434, 3348

Dale, D. A., Helou, G., Magdis, G. E., et al. 2014, ApJ, 784, 83

Dale, D. A., Cohen, S. A., Johnson, L. C., et al. 2009, ApJ, 703, 517

de Jong, R. S. 1996, A&A, 313, 377

de Vaucouleurs, G., de Vaucouleurs, A., Corwin, Jr., H. G., et al. 1991, Third Reference Catalogue of Bright Galaxies.

Dong, H., Calzetti, D., Regan, M., et al. 2008, AJ, 136, 479

Draine, B. T. 2003, ARA&A, 41, 241

D'Souza, R., Kauffman, G., Wang, J., & Vegetti, S. 2014, MNRAS, 443, 1433

Ferguson, A. M. N., Wyse, R. F. G., Gallagher, J. S., & Hunter, D. A. 1998, ApJ, 506, L19

Gawiser, E., Francke, H., Lai, K., et al. 2007, ApJ, 671, 278

Gil de Paz, A., Madore, B. F., Boissier, S., et al. 2005, ApJ, 627, L29

Gogarten, S. M., Dalcanton, J. J., Williams, B. F., et al. 2010, ApJ, 712, 858

González Delgado, R. M., Pérez, E., Cid Fernandes, R., et al. 2014, A&A, 562, A47

Governato, F., Willman, B., Mayer, L., et al. 2007, MNRAS, 374, 1479

Governato, F., Mayer, L., Wadsley, J., et al. 2004, ApJ, 607, 688

Herbert-Fort, S., Zaritsky, D., Moustakas, J., et al. 2012, ApJ, 754, 110

—. 2009, ApJ, 700, 1977

Ibata, R., Chapman, S., Ferguson, A. M. N., et al. 2005, ApJ, 634, 287

Kennicutt, Jr., R. C., Lee, J. C., Funes, José G., S. J., Sakai, S., & Akiyama, S. 2008, ApJS, 178, 247

Kennicutt, Jr., R. C., Armus, L., Bendo, G., et al. 2003, PASP, 115, 928

Krick, J. E., Bridge, C., Desai, V., et al. 2011, ApJ, 735, 76

Larson, R. B. 1976, MNRAS, 176, 31

Lee, K.-S., Dey, A., Reddy, N., et al. 2011, ApJ, 733, 99

Lee, S.-K., Ferguson, H. C., Somerville, R. S., Wiklind, T., & Giavalisco, M. 2010, ApJ, 725, 1644

Lee, S.-K., Idzi, R., Ferguson, H. C., et al. 2009, ApJS, 184, 100

Leitherer, C., Li, I.-H., Calzetti, D., & Heckman, T. M. 2002, ApJS, 140, 303

Liu, C.-Z., Shen, S.-Y., Shao, Z.-Y., et al. 2009, Research in Astronomy and Astrophysics, 9, 1119

MacArthur, L. A., Courteau, S., Bell, E., & Holtzman, J. A. 2004, ApJS, 152, 175

Martin, D. C., Fanson, J., Schiminovich, D., et al. 2005, ApJ, 619, L1

Martín-Navarro, I., Bakos, J., Trujillo, I., et al. 2012, MNRAS, 427, 1102

Michard, R. 2002, A&A, 384, 763

Monachesi, A., Bell, E. F., Radburn-Smith, D. J., et al. 2013, ApJ, 766, 106

Muñoz-Mateos, J. C., Gil de Paz, A., Boissier, S., et al. 2007, ApJ, 658, 1006

—. 2009, ApJ, 701, 1965

Noll, S., Burgarella, D., Giovannoli, E., et al. 2009, A&A, 507, 1793

Pahre, M. A., Ashby, M. L. N., Fazio, G. G., & Willner, S. P. 2004, ApJS, 154, 235

Papovich, C., Dickinson, M., & Ferguson, H. C. 2001, ApJ, 559, 620

Pierce, M. J., & Nations, H. L. 2002, in Bulletin of the American Astronomical Society, Vol. 34, American Astronomical Society Meeting Abstracts #200, 749

Pohlen, M., & Trujillo, I. 2006, A&A, 454, 759

Purcell, C. W., Bullock, J. S., & Zentner, A. R. 2007, ApJ, 666, 20

Radburn-Smith, D. J., Roškar, R., Debattista, V. P., et al. 2012, ApJ, 753, 138

Read, J. I., Pontzen, A. P., & Viel, M. 2006, MNRAS, 371, 885

Richards, E. 2015, MNRAS, in prep

Robertson, B., Bullock, J. S., Cox, T. J., et al. 2006, ApJ, 645, 986

Roškar, R., Debattista, V. P., Quinn, T. R., Stinson, G. S., & Wadsley, J. 2008, ApJ, 684, L79

Ryder, S. D., & Dopita, M. A. 1994, ApJ, 430, 142

Sánchez-Blázquez, P., Courty, S., Gibson, B. K., & Brook, C. B. 2009, MNRAS, 398, 591

Schaerer, D., de Barros, S., & Sklias, P. 2013, A&A, 549, A4

Schlafly, E. F., & Finkbeiner, D. P. 2011, ApJ, 737, 103

Sellwood, J. A., & Binney, J. J. 2002, MNRAS, 336, 785

Sheth, K., Regan, M., Hinz, J. L., et al. 2010, PASP, 122, 1397

Staudaher., S. 2015a, MNRAS, in prep

—. 2015b, MNRAS, in prep

Tal, T., & van Dokkum, P. G. 2011, ApJ, 731, 89

Thilker, D. A., Bianchi, L., Meurer, G., et al. 2007, ApJS, 173, 538

Tortora, C., Napolitano, N. R., Cardone, V. F., et al. 2010, MNRAS, 407, 144

van Zee, L., Dale, D. A., Barnes, K. L., et al. 2012, in American Astronomical Society Meeting Abstracts #220, 433.08

Wang, J., Kauffmann, G., Overzier, R., et al. 2011, MNRAS, 412, 1081

West, A. A., Garcia-Appadoo, D. A., Dalcanton, J. J., et al. 2009, AJ, 138, 796

Williams, B. F., Dalcanton, J. J., Dolphin, A. E., Holtzman, J., & Sarajedini, A. 2009, ApJ, 695, L15

Wright, E. L., Eisenhardt, P. R. M., Mainzer, A. K., et al. 2010, AJ, 140, 1868

Wu, H., Shao, Z., Mo, H. J., Xia, X., & Deng, Z. 2005, ApJ, 622, 244

York, D. G., Adelman, J., Anderson, Jr., J. E., et al. 2000, AJ, 120, 1579

Zhang, H.-X., Hunter, D. A., Elmegreen, B. G., Gao, Y., & Schruba, A. 2012, AJ, 143, 47

Zibetti, S., White, S. D. M., & Brinkmann, J. 2004, MNRAS, 347, 556

Table 1. Galaxy Sample

Galaxy	Alternative Name	α_0 & δ_0 (J2000)	Optical Morphology	$2a_{25} \times 2b_{25}$ ($' \times '$)	cz (km s^{-1})	A_V (mag)	P.A. (°)
NGC4220	UGC7290	121611.7+475300	SA0	3.89×1.36	914	0.049	139.7
UGC7301		121642.1+460444	Sd	1.82×0.24	690	0.030	81.6
NGC4242	UGC7323	121730.2+453709	SAB(s)dm	5.01×3.81	506	0.033	26.9
NGC4485	UGC7648	123031.1+414204	IB(s)m pec	2.29×1.63	493	0.059	3.8
NGC4490	UGC7651	123036.2+413838	SB(s)d pec	6.31×3.09	565	0.060	121.2
NGC4618	UGC7853	124132.8+410903	SB(rs)m	4.17×3.38	544	0.058	26.9
NGC4625	UGC7861	124152.7+411626	SAB(rs)m pec	2.19×1.90	621	0.050	133.4
NGC4707	DDO150	124822.9+510953	Sm?	2.24×2.08	468	0.030	23.1
UGC8303	HolmbergVIII	131317.6+361303	IAB(s)m	2.24×1.90	944	0.049	177.1
UGC8320	DDO168	131427.9+455509	IBm	3.63×1.38	192	0.042	149.9
NGC5055	Messier63	131549.3+420145	SA(rs)bc	12.59×7.18	484	0.048	94.0
NGC5229	UGC8550	133402.8+475456	SB(s)d?	3.31×0.56	364	0.049	166.8
NGC5273	UGC8675	134208.3+353915	SA0(s)	2.76×2.51	1085	0.028	3.5
NGC5523	UGC9119	141452.3+251903	SA(s)cd?	4.57×1.28	1039	0.052	92.0
NGC5608	UGC9219	142317.9+414633	Im?	2.63×1.34	663	0.026	94.9

Note. — The apertures used for the photometry have the centers and position angles (measured east of north) listed here, with ellipticities determined via b_{25}/a_{25}, where $2a_{25}$ and $2b_{25}$ are respectively the RC3 major axis and minor axis sizes of the B band isophote defined at 25 mag arcsec^{-2}. All information is taken from the NASA/IPAC Extragalactic Database (NED) including the foreground Milky Extinction.

Table 2. Imaging Integrations

Galaxy	*GALEX* FUV	*GALEX* NUV	WIRO u'	WIRO g'	WIRO r'	*Spitzer* 3.6 μm	WISE 12 μm	*Spitzer* 24 μm
NGC4220	12101	12101	3600	3600	3600	1800	72	10
UGC7301	13756	13757	3600	3600	3600	1800	72	72[a]
NGC4242	1683	3282	3600	3600	3600	1800	72	160
NGC4485	1587	2810	3600	3600	3600	1800	72	160
NGC4490	1587	2810	3600	3600	3600	1800	72	160
NGC4618	3242	3259	3600	3600	3600	1800	72	160
NGC4625	3259	3259	3600	3600	3600	1800	72	160
NGC4707	1664	1664	3600	3600	3600	1800	72	160
UGC8303	205	1623	3600	3600	3600	1800	72	72[a]
UGC8320	1576	3116	···	3600	3600	1800	72	160
NGC5055	3002	3754	···	3600	3600	1800	72	160
NGC5229	2757	2757	3600	3600	3600	1800	72	160
NGC5273	1659	1659	3600	3600	3600	1800	72	282[b]
NGC5523	96	96	3600	3600	3600	1800	72	72[a]
NGC5608	105	105	3600	3600	3600	1800	72	72[a]

Note. — Integrations are in seconds per position on the sky. The post-processing images utilized here have resolutions of $\approx 6''$ (GALEX, WISE 12 μm, Spitzer 24 μm, Herschel 70 μm), $1\farcs7$ (Spitzer 3.6 μm), and $2\farcs0$ (WIRO).

[a] *WISE* 22 μm

[b] *Herschel* 70 μm

Table 3. Fit Parameters

Parameter	Notation	Allowed Ranges
Metallicity	Z	0.008, 0.02, 0.05
IMF		Chabrier
Color excess: young stars	$E(B-V)^{\rm y}_*$	0.0, 0.025, 0.05, 0.1, 0.15, 0.2, 0.25, 0.3, 0.4
Color excess: old stars	$E(B-V)^{\rm o}_*$	$0.44E(B-V)^{\rm y}_*$
Dust emission template	α	0.5, 1.0, 1.25, 1.50, 1.75, 2.0, 2.25, 2.50, 3.00
Slope of power law that modifies attenuation curve	δ	-0.5, -0.4, -0.3, -0.2, -0.1, 0
Delayed Star Formation History		
SFR e-folding time (Gyr)	τ_0	0.5, 1, 2, 3, 4, 5, 6, 7, 10
Age of oldest stars (Gyr ago)	t_0	11
Double Exponential Star Formation History		
SFR e-folding time for older population (Gyr)	τ_1	0.5, 1, 2, 3, 4, 5, 6, 7, 10
Age of oldest stars for older population (Gyr ago)	t_1	11
SFR e-folding time for younger population (Gyr)	τ_2	10
Age of oldest stars for younger population (Gyr ago)	t_2	0.01, 0.03, 0.1, 0.3, 0.5
Mass fraction of the late burst	f_{ySP}	0.001, 0.01, 0.1, 0.2

Table 4. Integrated Fluxes

Galaxy	*GALEX* FUV	*GALEX* NUV	WIRO u'	WIRO g'	WIRO r'	*Spitzer* 3.6 μm	WISE 12 μm	*Spitzer* 24 μm
NGC4220	495±050E−1	143±014E+0	154±008E+1	712±036E+1	143±007E+2	197±010E+2	138±014E+2	148±010E+2
UGC7301	415±042E−1	566±057E−1	130±006E+0	344±017E+0	518±026E+0	307±015E+0	···	···
NGC4242	894±089E+0	141±014E+1	422±021E+1	123±006E+2	160±008E+2	120±006E+2	848±085E+1	105±007E+2
NGC4485	125±012E+1	164±016E+1	285±014E+1	572±029E+1	985±049E+1	415±021E+1	962±096E+1	201±014E+2
NGC4490	550±055E+1	876±088E+1	204±010E+2	453±023E+2	814±041E+2	514±026E+2	152±015E+3	427±030E+3
NGC4618	261±026E+1	335±033E+1	629±031E+1	159±008E+2	214±011E+2	165±008E+2	259±026E+2	395±028E+2
NGC4625	409±041E+0[c]	592±059E+0[c]	134±007E+1	345±017E+1	536±027E+1	480±024E+1	101±010E+2	127±009E+2
NGC4707	330±033E+0	375±038E+0	605±030E+0	137±007E+1	187±009E+1	974±049E+0	···	···
UGC8303	351±035E+0	423±042E+0	696±035E+0	174±009E+1	218±011E+1	122±006E+1	135±014E+1	512±036E+1[a]
UGC8320	533±053E+0	706±071E+0	···	280±014E+1	364±018E+1	168±008E+1	272±031E+0	102±009E+1
NGC5055	363±036E+1	658±066E+1	···	108±005E+3	188±009E+3	246±012E+3	499±050E+3	567±040E+3
NGC5229	183±018E+0	251±025E+0	533±027E+0	122±006E+1	185±009E+1	112±006E+1	464±047E+0	129±010E+1
NGC5273	230±026E−1	105±010E+0	156±008E+1	646±032E+1	127±006E+2	122±006E+2	417±042E+1	294±025E+3[b]
NGC5523	402±041E+0	588±059E+0	149±007E+1	390±019E+1	621±031E+1	525±026E+1	749±075E+1	131±009E+2[a]
NGC5608	322±032E+0	388±039E+0	655±033E+0	148±007E+1	199±010E+1	105±005E+1	295±031E+0	582±052E+0[a]

Note. — Fluxes (in mJy) are derived using $2a_{25} \times 2b_{25}$ elliptical apertures. The compact table entry format T.UV±W.XYEZ implies (T.UV±W.XY)×10^{Z}. All fluxes were corrected for Galactic extinction (Schlafly & Finkbeiner 2011) assuming $A_V/E(B-V) \approx 3.1$ and the reddening curve of Draine (2003). The uncertainties include both statistical and systematic effects. A color correction of 0.94 has been applied to the WISE 12 μm data (Wright et al. 2010).

[a] *WISE* 22 μm

[b] *Herschel* 70 μm

[c] Ultraviolet emission extends beyond the aperture (Thilker et al. 2007).

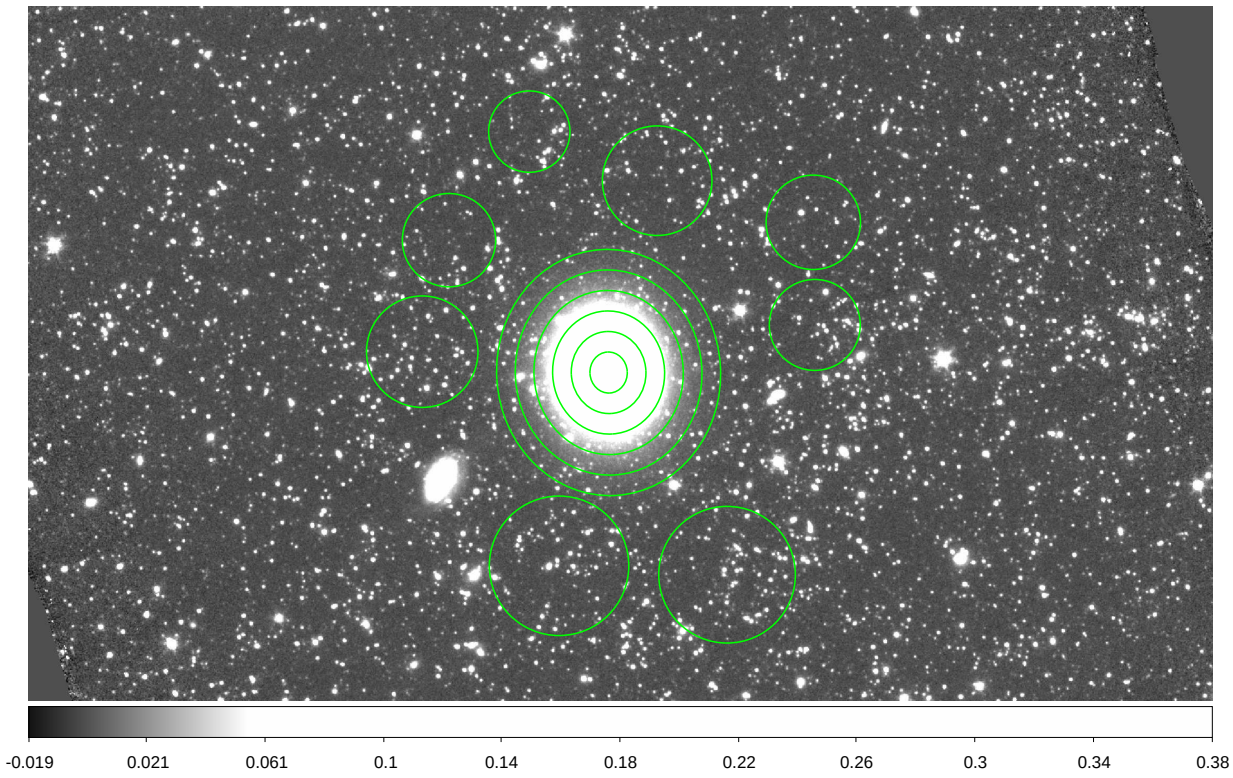

Fig. 1.— A 19′.9×11′.6 portion of the *Spitzer* 3.6 μm mosaic of NGC 5273. The ellipses demonstrate the annular regions for extracting photometry and the circles show the sky apertures purposefully chosen to include a representative sampling of foreground stars. North is up, East is to the left.

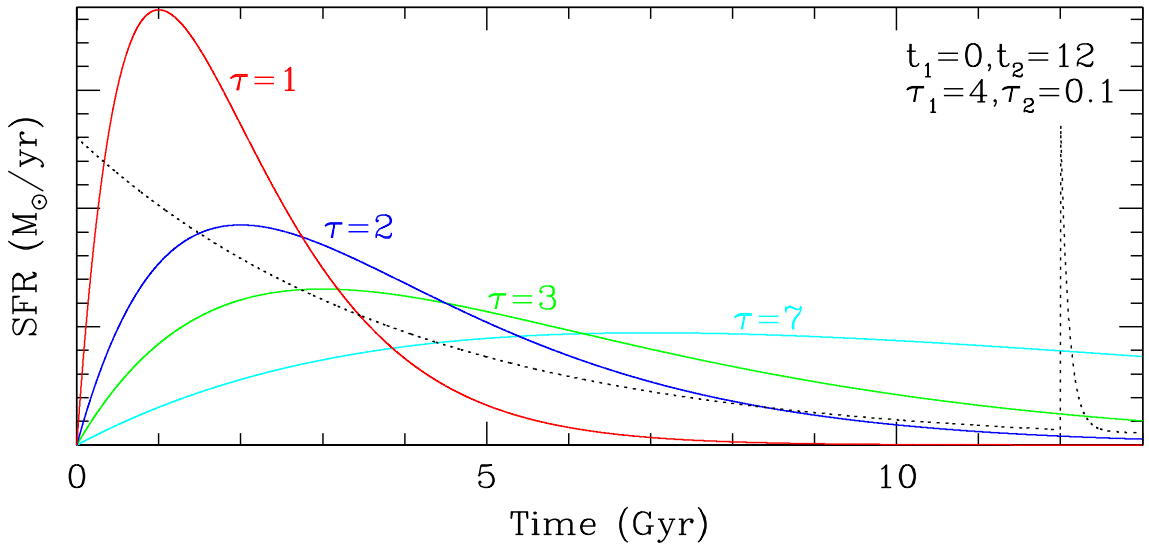

Fig. 2.— Four examples of a "delayed" star formation history along with one example of a double exponential star formation history (dotted curve). All values shown are in Gyr.

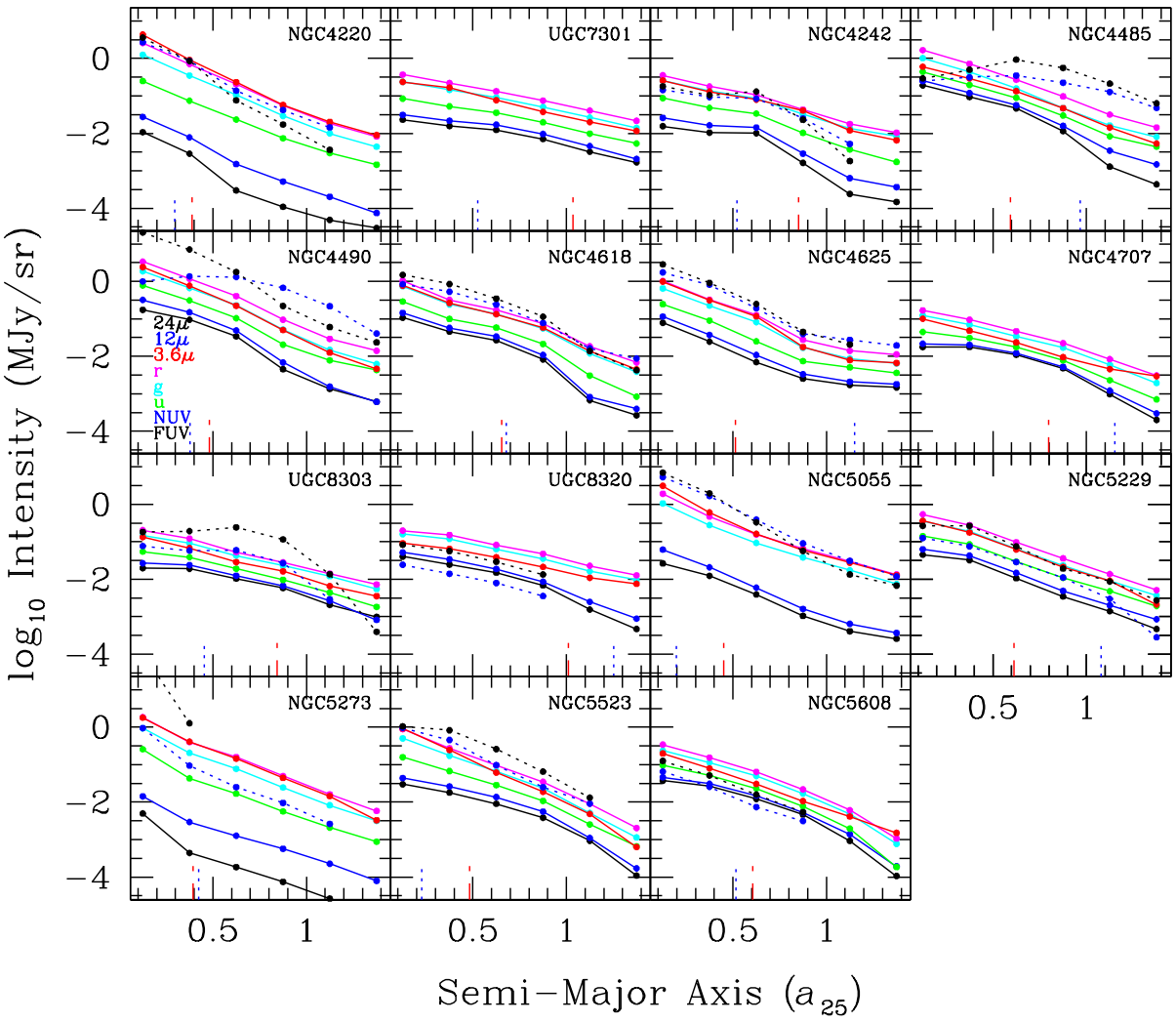

Fig. 3.— The observed multi-wavelength surface brightness profiles corrected for foreground Milky Way dust attenuation. The dotted curves are for dust emission, and the vertical dotted lines near the bottom of each panel indicate 3 kpc and the vertical dash-dot lines indicate twice the r' half-light radius.

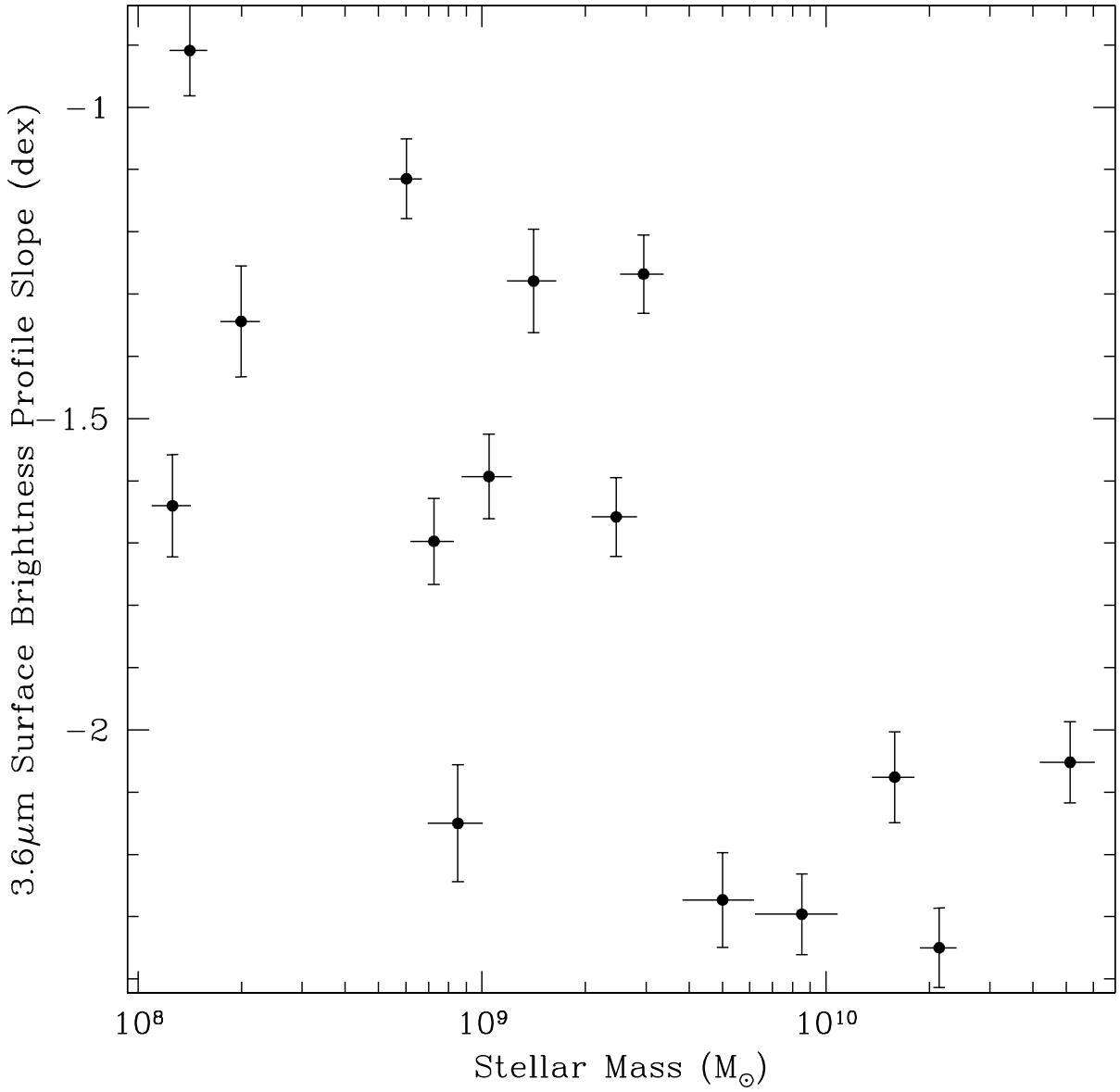

Fig. 4.— The slopes of 3.6 μm surface brightness profiles as a function of the stellar mass derived from the SED fitting described in § 4.2. The slopes are computed over $0 < a/a_{25} < 1.25$ and thus avoid the outermost annular data.

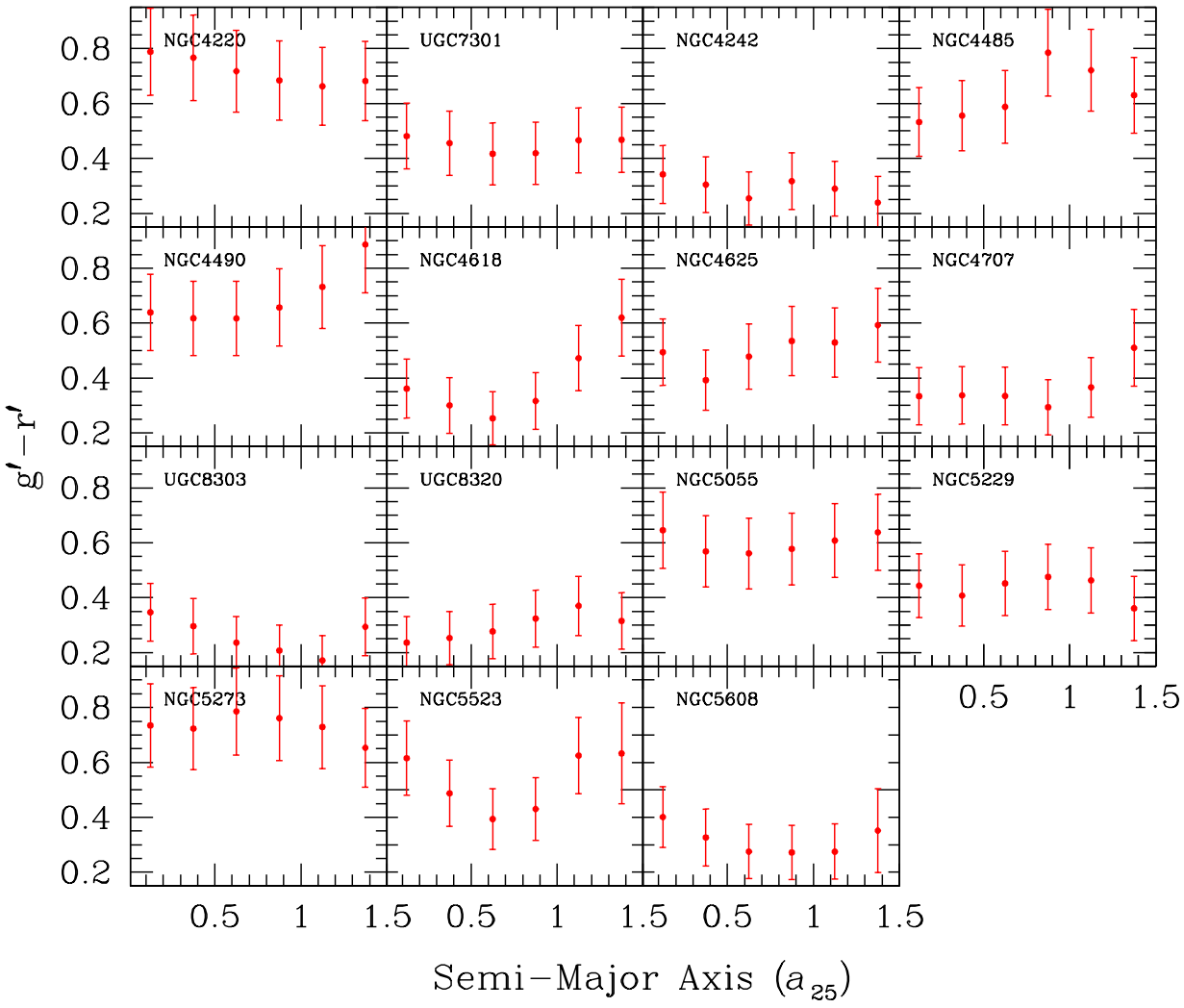

Fig. 5.— The $g' - r'$ color radial profiles.

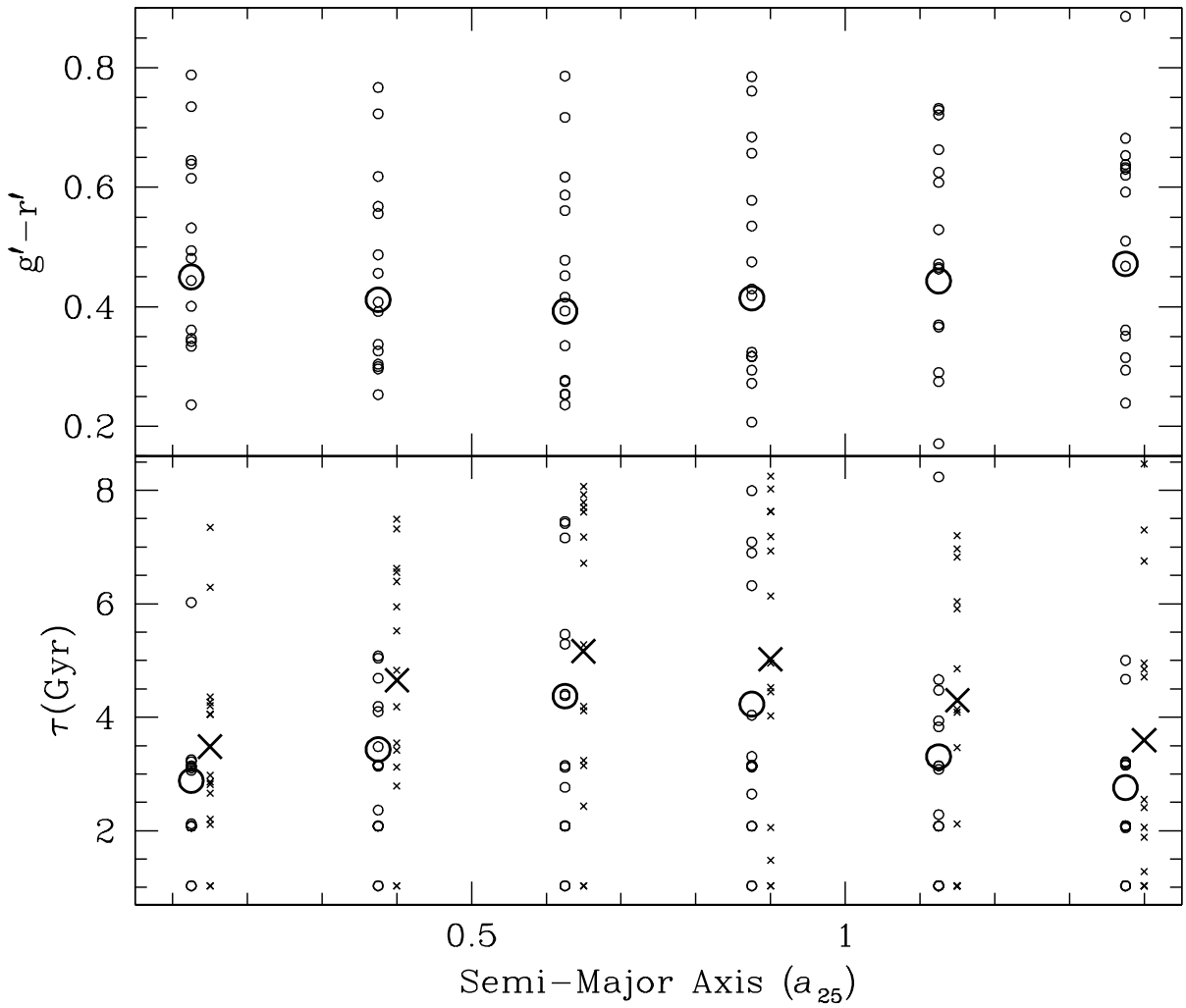

Fig. 6.— The distribution of $g'-r'$ and τ parameters. The large symbols indicate the average value for each radius; in the bottom panel the circles stem from a delayed star formation history and the (slightly offset for clarity) crosses represent the main stellar population in the double exponential star formation history model.

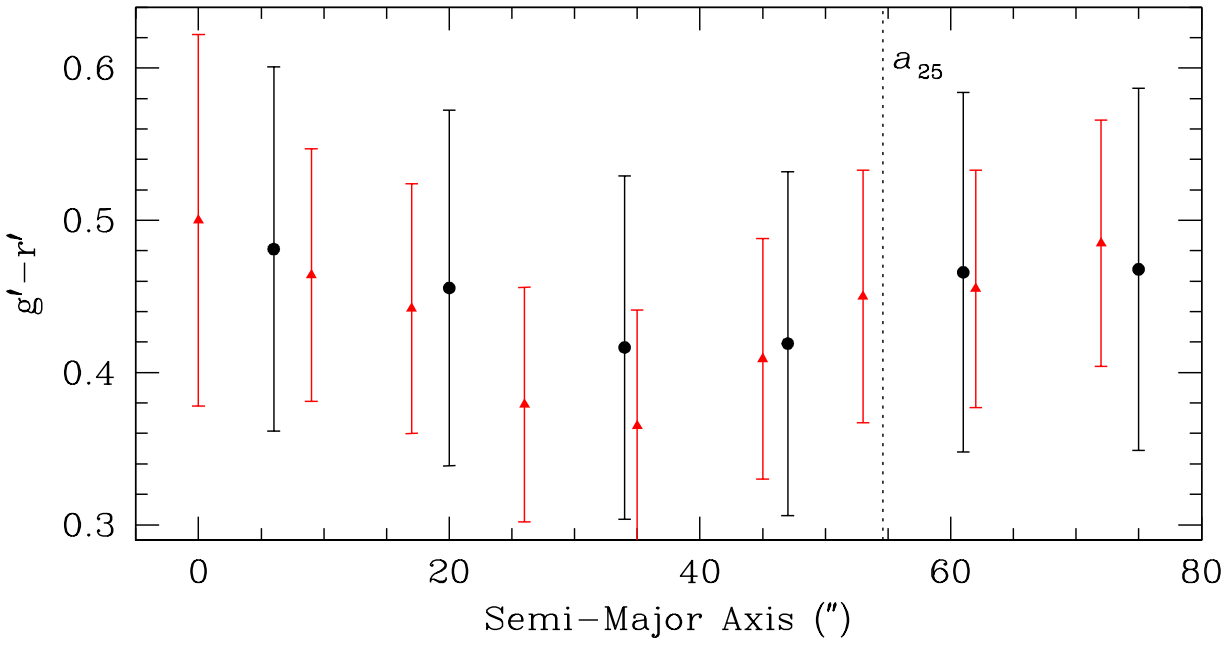

Fig. 7.— Comparison of annular-based optical colors (circles) with those derived from a series of 9″-diameter apertures placed along the major axis of UGC 7301 (triangles).

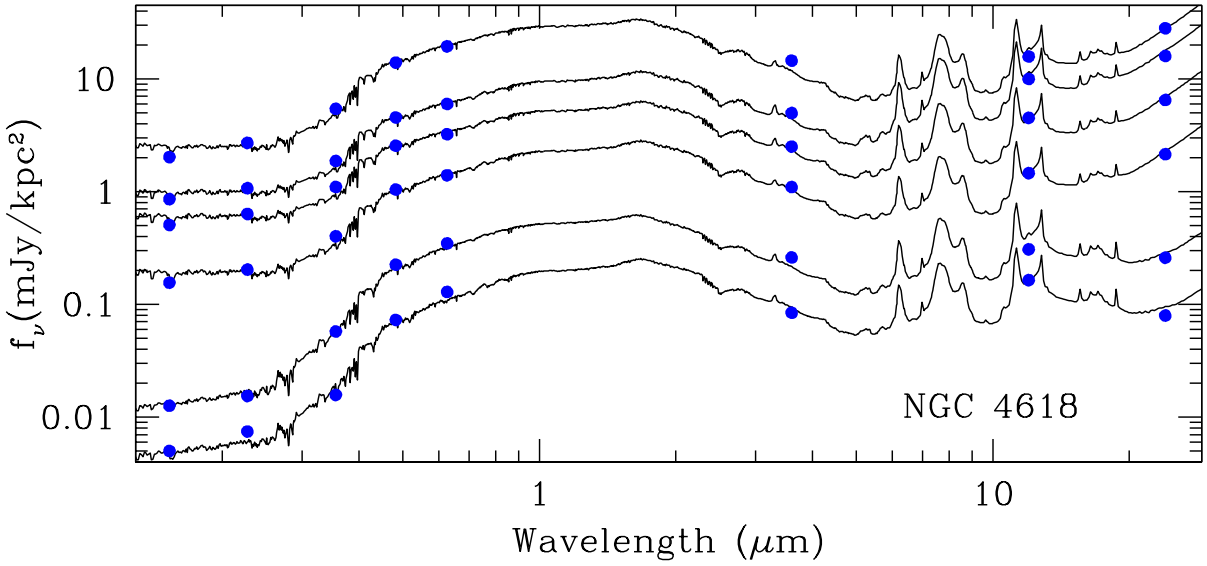

Fig. 8.— SEDs for the six annular regions of NGC 4618. The blue dots indicate the measured surface brightnesses and the black curves show the best-matched stellar+dust SEDs.

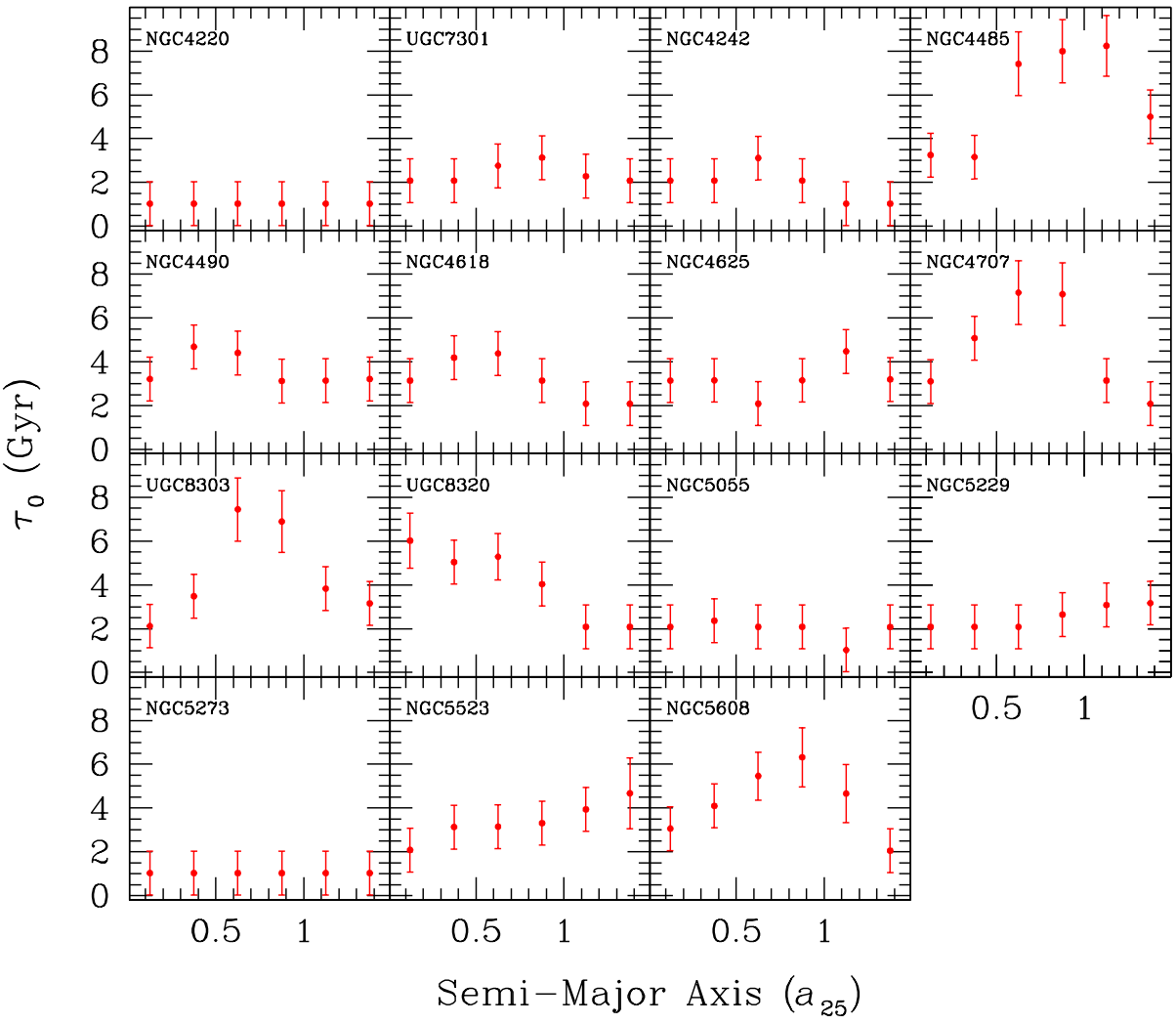

Fig. 9.— The e-folding τ_0 values assuming a delayed star formation history.

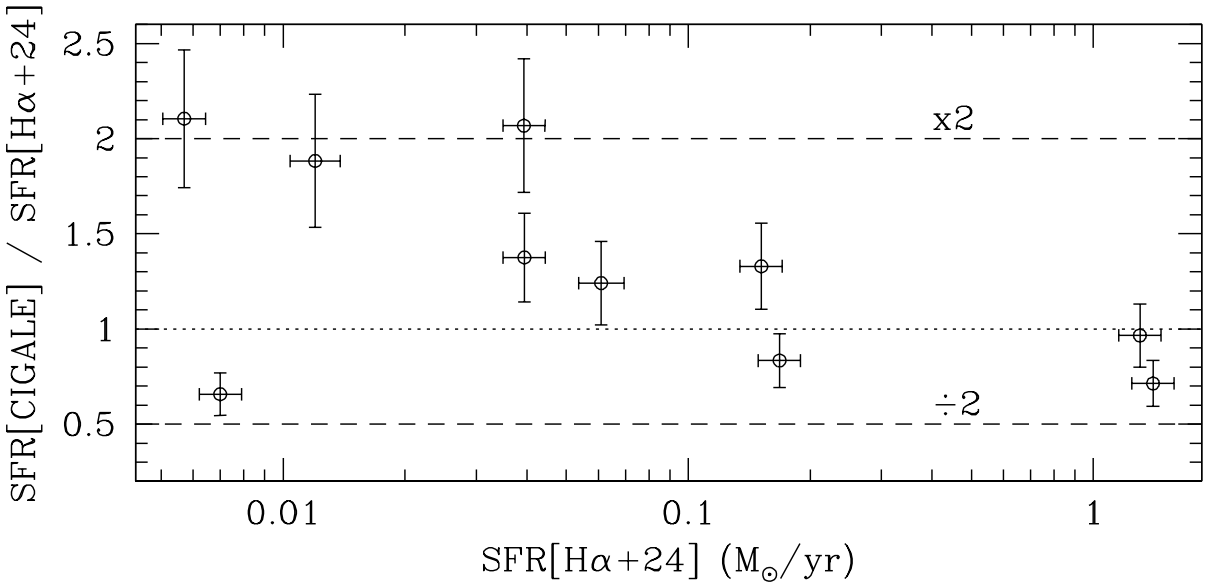

Fig. 10.— Comparison between the global star formation rates output by our CIGALE fits and those from a prescription that utilizes global Hα and 24 μm data.

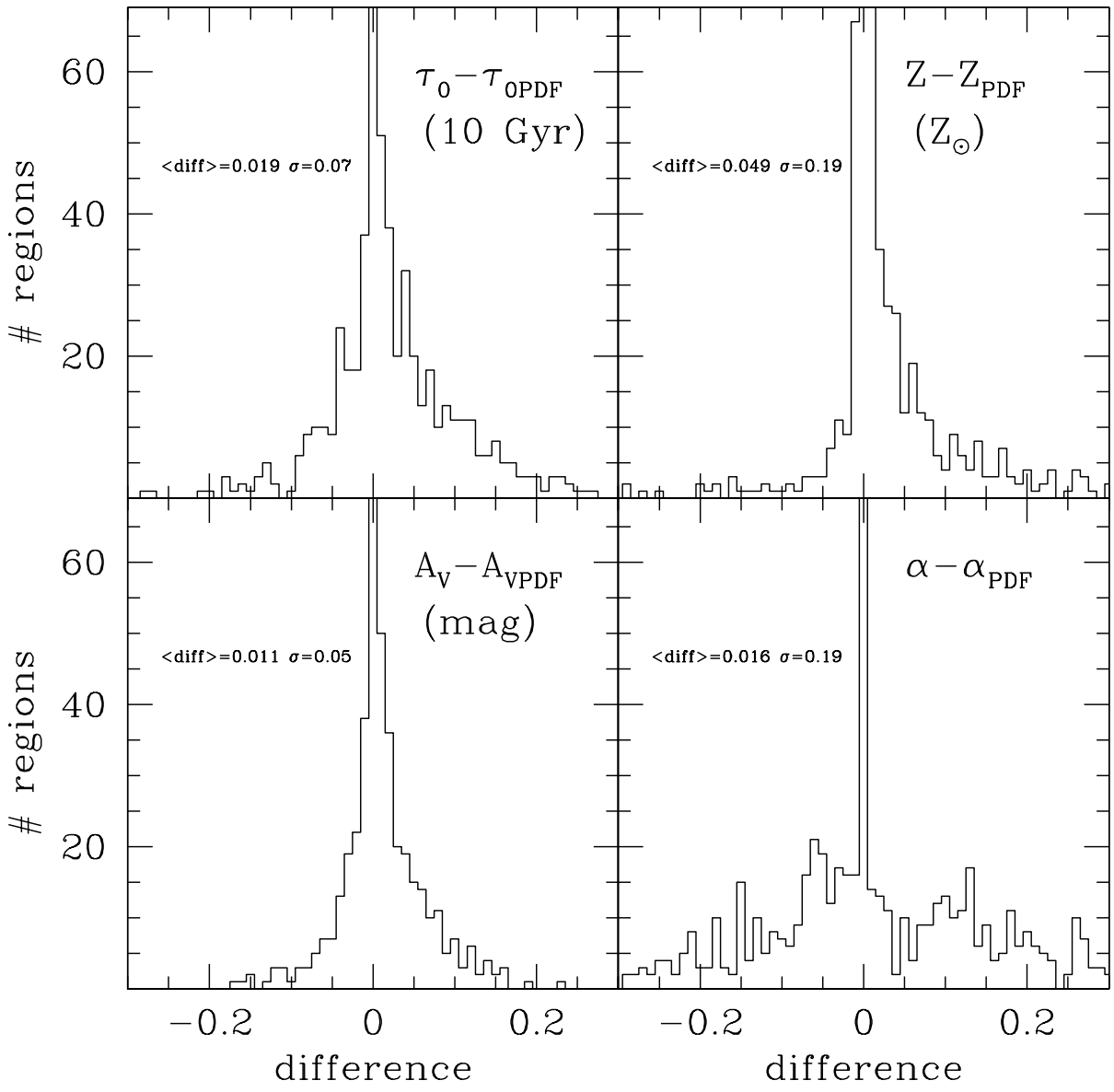

Fig. 11.— Comparison between Bayesian-based best-fit parameters with the fit results for a series of Monte Carlo simulations that inject uncertainty into the measured fluxes.